Title: Modulation of cation diffusion by reversible supramolecular assemblies in ionic liquid-based nanocomposites

Author: Vera Bocharova, Nishani Jayakody, Jie Yang, Robert L. Sacci, Wei Yang, Żaneta Wojnarowska [i in]

Citation style: Vera Bocharova, Nishani Jayakody, Jie Yang, Robert L. Sacci, Wei Yang, Żaneta Wojnarowska [i in]. (2020). Modulation of cation diffusion by reversible supramolecular assemblies in ionic liquid-based nanocomposites. "ACS Applied Materials Interfaces" iss. 28, (2020), s. 31842-31851.
DOI: 10.3390/ma13173696

ACS APPLIED MATERIALS & INTERFACES

www.acsami.org

Research Article

Modulation of Cation Diffusion by Reversible Supramolecular Assemblies in Ionic Liquid-Based Nanocomposites

Vera Bocharova,* Nishani Jayakody, Jie Yang, Robert L. Sacci, Wei Yang, Shiwang Cheng, Benjamin Doughty, Steven Greenbaum, Seung Pyo Jeong, Ivan Popov, Sheng Zhao, Catalin Gainaru, and Zaneta Wojnarowska*

Cite This: *ACS Appl. Mater. Interfaces* 2020, 12, 31842−31851

Read Online

ACCESS | Metrics & More | Article Recommendations

ABSTRACT: Ionic liquid (IL) properties, such as high ionic conductivity under ambient conditions combined with nontoxicity and nonflammability, make them important materials for future technologies. Despite high ion conductivity desired for battery applications, cation transport numbers in ILs are not sufficient enough to attain high power density batteries. Thus, developing novel approaches directed toward improvement of cation transport properties is required for the application of ILs in energy-storing devices. In this effort, we used various experimental techniques to demonstrate that the strategy of mixing ILs with ultrasmall (1.8 nm) nanoparticles (NPs) resulted in melt-processable composites with improved transport numbers for cations at room temperature. This significant enhancement in the transport number was attributed to the specific chemistry of NPs exhibiting a weaker cation and stronger anion coordination at ambient temperature. At high temperature, significantly weakened NP−anion associations promoted a liquid-like behavior of composites, highlighting the melt-processability of these composites. These results show that designing a reversible dynamic noncovalent NP−anion association controlled by the temperature may constitute an effective strategy to control ion diffusion. Our studies provide fundamental insights into mechanisms driving the charge transport and offer practical guidance for the design of melt-processable composites with an improved cation transport number under ambient conditions.

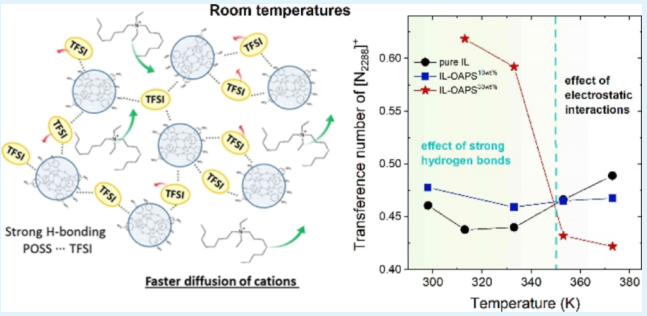

KEYWORDS: *nanocomposites, dynamic bonds, ionic conductivity, cation transport number, energy storage*

INTRODUCTION

Ionic liquids (ILs) are materials of great importance for various energy applications because of their high ionic conductivity.[1] However, a significant shortcoming of ILs is their relatively low cation transport number (t_+) (typically ~0.4)[2], which impedes their practical application. For instance, a small contribution of the cation to conductivity creates a significant gradient in ion concentration that leads to increased cell polarization, thereby reducing the power capability of a battery.[3,4] To advance the application of ILs in energy-harvesting and storage devices, the development of novel approaches leading to high cation transport numbers is desired.

The strategies toward increasing t_+ are related to anion immobilization through covalent or noncovalent interactions with polymers[4] and/or various ceramics.[5−12] Covalently attaching anions to polymers results in the transport number of cations close to unity,[4] yielding single-ion-conductive materials. However, compared to ILs, the significant drop in the conductivity observed for these polymers in the dry state constitutes a major limitation for their application. Although more efforts are underway with solid polymer electrolytes, alternative commercially viable strategies include the development of single-ion-conducting gel polymer electrolytes, which show both high conductivity and high ion transport number. However, only a few examples of such materials[13,14] are available in the literature.

The effect of covalent and noncovalent interactions between the cation and ceramics has been a topic of extensive research.[15] One of the successful examples of covalently immobilized anion that have relatively high conductivity (4×10^{-4} S/cm at 343 K) and high cation transport number in the dry state has been reported for cografting bis-(trifluoromethanesulfonyl)imide (TFSI) anions and strands of polyethylene oxide (PEO) to aluminum and silica

Received: May 6, 2020
Accepted: June 22, 2020
Published: June 22, 2020

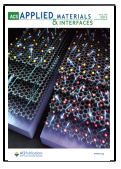

https://dx.doi.org/10.1021/acsami.0c08323
ACS Appl. Mater. Interfaces 2020, 12, 31842−31851

nanoparticles (NPs).[5] Furthermore, not only covalent attachment but also the physical blending of ionic materials with ceramics has been shown to significantly improve the cation transport number.[16−18] For example, Croce et al.[16] reported that depending on the acidity of the ceramics, the value of transport number of Li for a PEO/$LiClO_4$-based polymer composite can be improved from 0.25 to 0.5−0.6 for acidic TiO_2 particles while for less acidic Al_2O_3 particles, a modest increase from 0.25 to 0.3 is observed. Although the improvement of the cation transport number for polymer electrolytes in the presence of ceramics is supported by the literature,[15] much less is known about the same effect in ILs. Nevertheless, the findings in the field of polymer electrolyte-based composites identify that the interfaces between the inert ceramic and polymer electrolytes might play a significant role in the improvement of the transport properties of the cation. In this respect, the utilization of smaller particles (below 100 nm) which have a large surface area might benefit the transport properties of the cation. However, the addition of NPs has raised concerns about material processability. For instance, in IL-based composites with nonconductive NPs, the high ionic conductivity is achieved only with NP concentration not exceeding 10 wt %,[19,20] while further i-increasing the concentration of NPs ultimately leads to a degradation in the mechanical and conductive properties.

Given the performance trade-offs between ion conductivity, processability, and transport number in various polymer and composite materials, it is important to design a hybrid structure that will be easily processable and combine the high transport number of single-ion-conducting polymers with the high conductivity of ILs.

In this paper, we pursue the strategy of adding ultrasmall octaaminophenyl silsesquioxane (OAPS) NPs ($D \sim 1.8$ nm)[21] to the dioctyldiethylammonium (bis-(trifluoromethanesulfonyl)imide) (N_{2288} TFSI) IL to design a melt-processable composite with an improved transport number of the cation. The selection of these NPs is driven by their large surface area and unique surface chemistry capable to form noncovalent interaction with the ions in ILs. Additionally, their size was selected based on the literature reports[21,22] demonstrating that ultrasmall filler sizes aid composite processability. To characterize the IL−OAPS composites, the combination of several experimental techniques including broadband dielectric spectroscopy (BDS), pulse field gradient nuclear magnetic resonance (PFG-NMR), differential scanning calorimetry (DSC), Fourier transform infrared (FTIR) spectroscopy, and shear rheology was used. Using this approach, we found that the transport number of cations can be improved up to ∼40% at 40 °C. From rheology and FTIR spectroscopy, the formation of a dynamic supramolecular network has been observed that was shown to control the transport of the ions. The corresponding switch in the transport number of ions was found to coincide with the onset of the decoupling between the ion conductivity obtained from BDS and the structural relaxation probed with rheology. The latter finding can shed new light on the mechanism leading to the decoupling of ion transport from the structural rearrangements. This phenomenon plays an important role in ion transport in superionic ceramics,[23−25] and is responsible for the high conductivity observed in the glassy state. Evidence of decoupling has been reported also for organic ionic materials, e.g. mostly polymer electrolytes.[26−34] To the best of our knowledge, the currently examined case is among a few known reports[35,36] where the decoupling between charge transport and structural relaxation has been found in low-molecular-weight (MW) aprotic ILs. Understanding and nourishing this mechanism in IL composites might be effective in designing the new generation of batteries.

EXPERIMENTAL DETAILS

Materials and Methods. OAPS NPs were purchased from Mayaterials. The N_{2288} TFSI IL was purchased from IoLiTec. All materials were used as received, that is, without further purification.

The OAPS particle and the IL were individually dissolved in tetrahydrofuran (THF). Based on the weight ratio, the OAPS/THF solution was added dropwise to the IL/THF solution while stirring. The mixture was stirred for more than an hour in a closed container, followed by the slow solvent evaporation after the lid was removed. The samples were dried in an oven at 110 °C for 24 h to remove the residual solvent and water before the measurements. The volume fractions of OAPS in nanocomposites were obtained by thermogravimetric analysis (TGA, performed with a Q50 device from TA Instruments using a cooling rate of 20 K/min, under air) from the weight loss between 403 and 1073 K.

DSC Measurements. The calorimetric tests of the studied samples were performed using a Mettler Toledo DSC1STAR System equipped with a liquid nitrogen cooling accessory and an HSS8 ceramic sensor (a heat flux sensor with 120 thermocouples). The sample was measured in aluminum pans with a 40 μL volume. Before the measurements, the samples were annealed for 15 min at 373 K. Then, heating from 143 to 373 K at a rate of 10 K/min was performed. During the experiments, the flow of nitrogen was maintained at 60 mL/min.

Broadband Dielectric Spectroscopy. The dielectric spectra were collected in the frequency range of 10^{-1} to 10^{7} Hz using a Novocontrol system that included an Alpha-A Impedance Analyzer and a Quattro Cryosystem temperature control unit. The samples were measured using a parallel-plate dielectric cell made of invar and sapphire.[37] The separation between the electrodes was maintained at 47 μm which yielded a geometrical capacitance of 21 pF. The measurements were performed from high to low temperatures. The dielectric cell was placed inside the cryostat with a nitrogen atmosphere and equilibrated at 380 K for at least 1 h. The experimental results were reproducible, which indicated the samples did not degrade upon heating and contained no residual solvent. Before acquiring the dielectric spectra, the samples were equilibrated for at least 15 min to achieve thermal stabilization within 0.2 K after each temperature step. Additional technical details regarding the measurements with BDS can be found in ref 38.

Measurements of Density. The mass of the samples was measured using a weight balance (Mettler Toledo NewClassic MF model MS105DU) with an accuracy of 0.01 mg. The gas pycnometer (Micromeretics Accupyc II 1340) measured the volume of penetrable helium gas within the sample and sample cup (total volume 0.1 cm^3) until the pressure did not vary more than 0.005 psig/min during the equilibration period. The accuracy of the volume measurement is 0.0001 cm^3. This cycle was repeated five times for reproducibility. The density was then determined from the mass-to-volume ratio, and the error of this measurement is less than 0.3%. All the density data were obtained at atmospheric pressure and $T = 293$ K.

Rheology Measurements. The rheological measurements of IL−OAPS nanocomposites were performed on an Anton Paar MCR302 with a CTD600 environmental chamber and an EVU20 evaporation unit. The temperature control had an accuracy of ±0.1 K. Small amplitude oscillatory shear (SAOS) with a strain amplitude, γ, of 0.1% has been performed at angular frequencies between 10^{2} and 10^{-1} rad/s on a pair of parallel plates with a diameter of 8 mm. For each sample, we measured the SAOS spectra at temperatures from the glass transition temperature T_g up to T_g + 100 K. The linear viscoelastic spectra master curves over a wide frequency region were constructed by employing the frequency−temperature superposition. To directly determine the steady-state (zero) shear viscosity of the IL

https://dx.doi.org/10.1021/acsami.0c08323
ACS Appl. Mater. Interfaces 2020, 12, 31842−31851

and composites, creep experiments were carried out in the same geometry with an applied stress of 100 Pa at high temperatures and up to 10,000 Pa at temperatures close to T_g.

FTIR Spectroscopy. Temperature effects on infrared adsorption were measured using an Agilent Cary 680 FTIR spectrometer equipped with a heated attenuated total reflection stage (Specac, GoldenGate). The interferometer mirror speed was 5 kHz, the resolution was set to 4 cm^{-1}, and 258 scans were integrated for the sample and backgrounds. The sample was allowed to equilibrate for 15 min at the given temperature before measurement. The temperature was scanned in both directions and the spectra showed less than 5% difference between the scans.

PFG-NMR Measurements. The PFG spin-echo sequence was applied to measure the individual diffusion coefficients of ^1H and ^{19}F nuclei. The measurements were carried out at 298, 313, 333, 353, and 373 K using a Varian Direct Digital Drive NMR spectrometer operating at 300 MHz for proton and 283 MHz for ^{19}F and using a DOTY Z-spec diffusion probe and gradient driver with a maximum field gradient of 1200 G/cm. The duration of the gradient pulsedelta and the interval between two pulsesdelta ranged from 1−4 to 100 ms, respectively. The gradient strength, g, was varied for each experiment (32 values, linear increase, g = 0−1200 G/cm). The self-diffusion coefficients, D, were then extracted by fitting the decay echo signal with the Stejskal−Tanner equation

$$I = I_0 \exp[-D\delta^2 g^2 \gamma^2 (\Delta - \delta/3)]$$

where I is the amplitude of the attenuated echo signal, I_0 is the initial intensity, and γ is the gyromagnetic ratio.

RESULTS

The chemical structures of the IL and OAPS are presented in Figure 1 while their physicochemical characteristics are collected in Table 1.

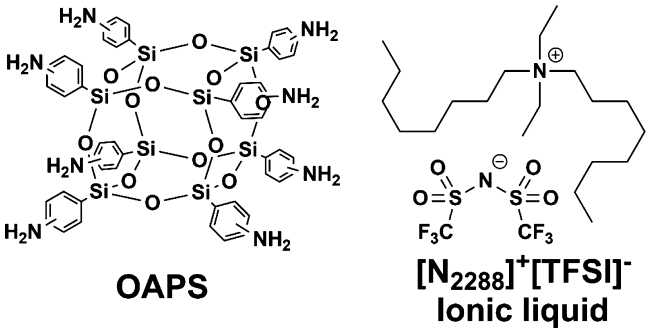

Figure 1. Chemical structures of OAPS NPs and the IL.

Thermal Characteristics of the Studied Materials. DSC was used to assess the glass transition temperature of the composites. The corresponding thermograms are presented in Figure 2 with the T_g values summarized in Table 1. As can be seen, the increase in OAPS concentration leads to an increase in T_g (Table 1) and to a substantial broadening of the glass transition step (inset of Figure 2). The latter is associated with

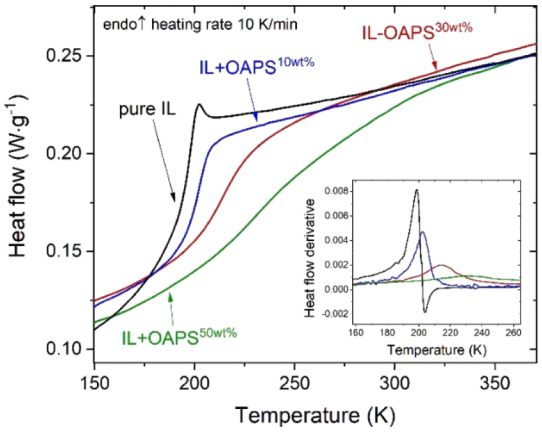

Figure 2. DSC thermograms of the investigated samples. The inset presents a derivative of heat flow plotted as a function of temperature.

the increasing distribution of segmental relaxation times of the IL in the composite that arises because of heterogeneity that scales with an increase in particle concentration.

Conductive and Viscoelastic Properties of Studied Samples. The dielectric data of pure IL and IL−OAPS composites were gathered over a wide temperature range. The results obtained for IL−OAPS$^{30\ wt\ \%}$ are presented in conductivity and modulus terms in Figure 3A,B, respectively.

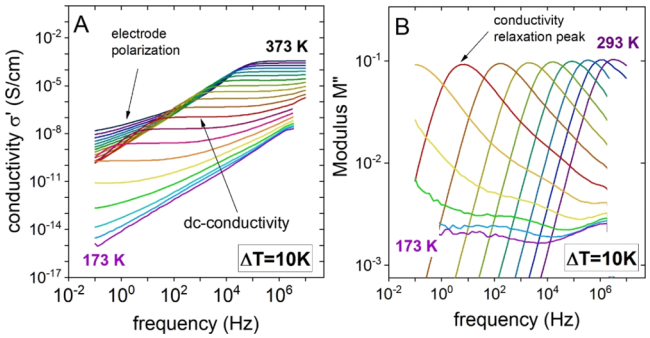

Figure 3. (A) Real part of the conductivity spectra for IL−OAPS$^{30\ wt\ \%}$. The plateau level was used to estimate the dc conductivity $\sigma_{dc}(T)$. (B) Imaginary part of the dielectric modulus, with the peak position providing the characteristic time of ion relaxation.

The conductivity spectra exhibit typical behavior for ionic materials with a frequency-dependent ac conductivity at higher frequencies, followed by a dc conductivity plateau σ_{dc}, and further by a large decrease because of electrode polarization effects at lower frequencies.[39] The AC−DC transition is visible in the imaginary part of the electric modulus (M'') representation as a well-resolved peak with the maximum

Table 1. Physical Properties of the Studied Composites[a]

sample	ρ, g/cm^3	T_g, K	σ_{dc} at T_g S/cm	wt % OAPS	σ_{dc} at 333 K S/cm	t_+/t_- (333 K)
pure IL	1.20	196	1×10^{-15}	0	8.55×10^{-4}	0.44/0.56
IL−OAPS$^{10\ wt\ \%}$	1.22	200	1×10^{-15}	10	4.3×10^{-4}	0.48/0.52
IL−OAPS$^{30\ wt\ \%}$	1.30	215	2.5×10^{-14}	30	7.7×10^{-5}	0.59/0.41
IL−OAPS$^{50\ wt\ \%}$	1.51	247	4×10^{-13}	50	2.3×10^{-5}	n/a

[a]TGA was used to estimate the weight fraction of OAPS. T_g was measured by DSC. BDS was used to measure the dc conductivity, and the results of PFG-NMR were used to estimate the transport number of cations/anions (t_+/t_-).

https://dx.doi.org/10.1021/acsami.0c08323
ACS Appl. Mater. Interfaces 2020, 12, 31842−31851

defining the conductivity relaxation time, $\tau_\sigma = 1/2\pi f_{max}$. Upon decreasing the temperature, the $M''(f)$ peak shifts toward lower frequencies and moves out of the experimental frequency window below the calorimetric T_g.

In ILs, the (dipolar) structural relaxation cannot be accessed via BDS because of the high ion conductivity; therefore, rheology was employed to extract the structural relaxation time and the viscosity of the studied systems. The mechanical data of IL−OAPS$^{30\ wt\ \%}$ in the form of master plots are presented in Figure 4. The horizontal shift factors employed to construct

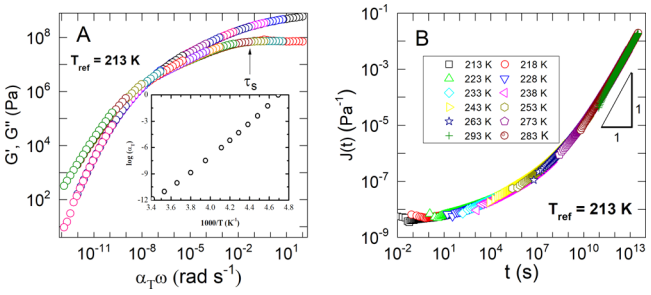

Figure 4. (A) G' and G'' master plots accessed from shear rheology for IL−OAPS$^{30\ wt\ \%}$; (B) creep compliance master plot of the IL−OAPS$^{30\ wt\ \%}$ nanocomposite.

the master plot of the shear modulus components $G'(\omega)$ and $G''(\omega)$ are presented in the inset of Figure 4A. In the following, the structural relaxation time τ_s refers to the characteristic time of the high-frequency loss peak observed for $G''(\omega)$, as shown in Figure 4A, reaching the calorimetric T_g value of about 100 s. The zero shear viscosity was extracted from the creep compliance $J(t)$ data (Figure 4B). The slope of unity at a long time indicates the long-range flow regime of IL−OAPS$^{30\ wt\ \%}$. The IL−OAPS$^{50\ wt\ \%}$ sample was measured only with the creep compliance, $J(t)$, while the other (modulus) rheological measurements were difficult to implement because of the high stiffness of this material. Nevertheless, the $J(t)$ measured at the constant stress contains the same set of dynamic information as the linear viscoelastic spectra of the storage modulus measured from the SAOS.[40]

Diffusion Measurements. PFG-NMR measurements were used to study the diffusion of ions in pure IL, IL−OAPS$^{10\ wt\ \%}$, and IL−OAPS$^{30\ wt\ \%}$. The diffusion coefficient of ions in the IL−OAPS$^{50\ wt\ \%}$ sample, as well as that of OAPS NPs, could not be measured because of their low mobility. The results of NMR measurements for the diffusion coefficients of ^{1}H and ^{19}F nuclei, a representative for cations and anions, respectively, are presented in Figure 5 and discussed below.

DISCUSSION

Charge Transport in the Supercooled Liquid State. The dc conductivity data of all studied materials are presented in Figure 5A. As recognized here, there are two characteristic regions separated by T_g, and the conductivity at T_g is marked with colored horizontal arrows. Above T_g, the dc conductivity follows the Vogel−Fulcher−Tamman (VFT) behavior, while below T_g, it can be described by the Arrhenius equation. Overall, under any constant T-condition, the dc conductivity decreases with the increase in OAPS concentration, that is, it becomes more and more separated from σ_{dc} corresponding to the pure IL.

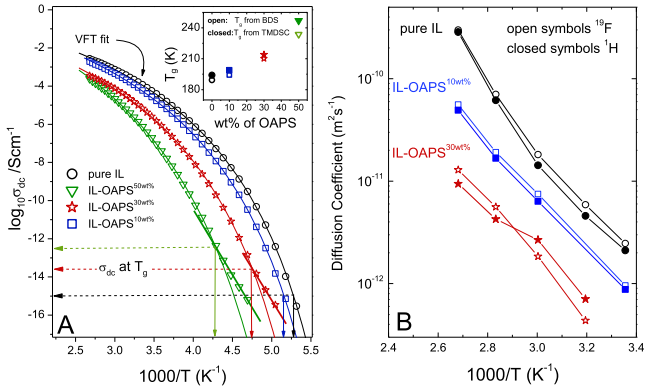

Figure 5. (A) Temperature dependence of dc conductivity in IL and IL−OAPS samples estimated from the dc plateau of BSD spectra similar to those presented in Figure 1A. Above T_g, the conductivity follows a VFT-like behavior, $\sigma_{dc} \propto \exp[DT_0/(T - T_0)]$, while below T_g, it follows an Arrhenius-type, $\sigma_{dc} \propto \exp(-E_a/k_BT)$ with E_a = 114 and 129 kJ/mol for IL−OAPS$^{50\ wt\ \%}$ and IL−OAPS$^{30\ wt\ \%}$, respectively. The vertical arrows indicate the dc conductivities at T_g. The inset presents the comparison between T_g values determined from the conductivity measurements and DSC. (B) Diffusion coefficient measured by PFG-NMR for pure IL and IL−OAPS mixtures.

Because the dc conductivity is directly related to the number of ions and their mobility, the observations coming from the BDS technique should be also reflected in ion diffusion. As depicted in Figure 5B, the ion diffusivity measured by PFG-NMR slows down with an increase in OAPS concentration. Additionally, for IL−OAPS$^{30\ wt\ \%}$, in the temperature range above 350 K, cations diffuse slower than anions, resembling the diffusive behavior of ions in the pure IL. The slower diffusion of the $[N_{2288}]^+$ cation can be assigned to its large size further influenced by the ability of the alkyl tail (Figure 1) to form self-assembled structures.[41,42] In the temperature regime below 350 K, the diffusivity of anions in IL−OAPS$^{30\ wt\ \%}$ drops below that of cations. Such an unexpected switch in the diffusion coefficient reflects some changes in the diffusive environment with the increase in the OAPS concentration. Indeed, some evidence of heterogeneity growth in the composites with an increase in the concentration of OAPS exists in broadening of the glass transition temperature step (Figure 2) observed from DSC.

Overall, our analysis of conductivity and diffusivity shows that they both decrease with the increase in the OAPS concentration. To understand the underlying mechanism of this decrease, we examine the effect of the glass transition temperature on the conductive behavior. This dynamic parameter affects the conductivity in the systems in which the structural relaxation directly controls ion transport. Such a coupling between conductivity and structural relaxation has been reported for many aprotic ILs.[43−45] As shown in the inset of Figure 5A, the addition of OAPS NPs leads to an increase in T_g. From scaling the conductivity plot in Figure 5A by T_g (Figure 6A), it can be seen that the conductivity data at high T nearly coincide with each other, suggesting that, indeed, in this temperature range, the T_g parameter is the major driver of the conductivity changes.

Ion Dynamics in the Vicinity of Liquid−Glass Transition. The same T_g-based argument, however, cannot be used to explain behavior in the region near T_g (see Figure 6A), where the conductivity data for the composites strongly

https://dx.doi.org/10.1021/acsami.0c08323
ACS Appl. Mater. Interfaces 2020, 12, 31842−31851

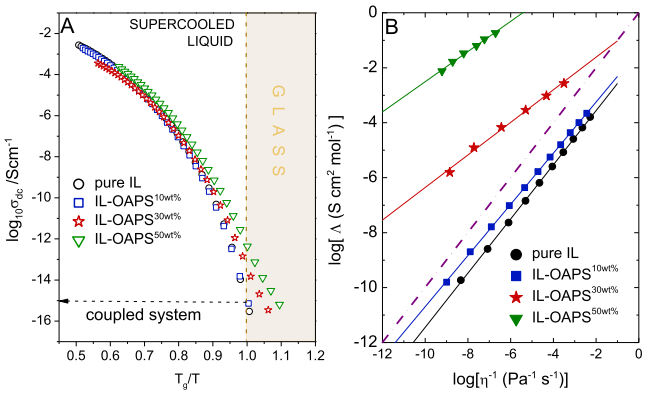

Figure 6. (A) dc conductivity as a function of T_g/T. (B) Walden plot of IL and IL−OAPS composites. The solid lines are linear fits of the data. For reference, the purple dot-dashed line presents the conductivity of the diluted solution of KCl to demonstrate the behavior of an ideal electrolyte.

deviate from the IL curve. This is especially noticeable for the IL−OAPS$^{30\ wt\ \%}$ and IL−OAPS$^{50\ wt\ \%}$ composites.

For the studied composites, different values of σ_{dc} are observed at T_g (Figure 6A). Specifically, $\sigma_{dc}(T_g)$ is $\sim 4 \times 10^{-13}$, $\sim 2.5 \times 10^{-14}$, $\sim 1 \times 10^{-15}$, and $\sim 10^{-15}$ S/cm for IL−OAPS$^{50\ wt\ \%}$, IL−OAPS$^{30\ wt\ \%}$, IL−OAPS$^{10\ wt\ \%}$, and pure IL, respectively. According to the literature,[46] $\sigma_{dc}(T_g) \sim 10^{-15}$ S/cm indicates that the charge transport is fully coupled to structural relaxation in an ionic system. This situation is observed in the case of pure IL and IL−OAPS$^{10\ wt\ \%}$. The remaining composites exhibit σ_{dc} at T_g higher than that of fully coupled systems. This indicates that the samples with high OAPS concentration exhibit different degrees of decoupling of ion transport from structural dynamics. To quantify the magnitude of such a phenomenon, we use the decoupling index defined as $R_\sigma(T_g) = 15 + \log \sigma_{dc}(T_g)$.[47,48] This simple approach is often used to estimate the degree of decoupling for various ionic systems without a direct viscoelastic characterization of the materials.[49] For our systems, the largest degree of decoupling [with $R_\sigma(T_g) = 6$] is found for IL−OAPS$^{50\ wt\ \%}$; for IL−OAPS$^{30\ wt\ \%}$, this value is smaller and equal to 1.4, while pure IL and IL−OAPS$^{10\ wt\ \%}$ practically follow the behavior of fully coupled systems. An alternative method to quantify the decoupling phenomenon is based on the joint analysis of conducting and viscoelastic properties of a given system in terms of the Walden plot. A significant advantage of this approach is the possibility to investigate the decoupling between structural dynamics and ion transport not only at T_g, as is the case for $R_\sigma(T_g)$, but also over a broad temperature range.

Figure 6B represents the Walden plot where the "ideal" line corresponds to the case of complete coupling of ion conductivity to structural relaxation and a full dissociation of all ion pairs. It has the slope equal to 1 that corresponds to the case of the molar conductivity $\Lambda \propto \eta^{-1}$ (the steady-state viscosity), and it is well-obeyed by the conductivity of K^+ in dilute aqueous solutions (dot-dashed line in Figure 6B). The data above this line correspond to a "superionic" regime, with ionic motions faster than structural relaxation, while the data below the ideal line usually indicate a poor dissociation of ion pairs. In the case of the Walden plot analysis, the decoupling between ion conductivity and structural relaxation is characterized by the exponent α estimated from the power-law behavior $\Lambda \propto \eta^{-\alpha}$, where α is the slope in the corresponding double-logarithmic plot which is connected to the decoupling exponent as $\varepsilon = 1 - \alpha$. Our data demonstrate that in IL and IL−OAPS$^{10\ wt\ \%}$, the conductivity is coupled to structural relaxation, as the slope is very similar to that of the ideal case ($\varepsilon = 0$). Such a behavior is in line with the behavior of most aprotic ILs which show vehicle-type conduction. On the other hand, a high concentration of OAPS renders the corresponding systems strongly decoupled over a broad temperature range, in which the charge transport *becomes faster than structural dynamics*. The decoupling is the strongest and extends over the broadest temperature range in IL−OAPS$^{50\ wt\ \%}$. The decoupling exponent, ε, reached 0.5 for IL−OAPS$^{50\ wt\ \%}$, which, to our knowledge, represents the strongest decoupling reported for IL-containing materials. For comparison, the decoupling exponent of ILs reported in refs 35 and 36 is only ~0.1. Interestingly, for the case of IL−OAPS$^{30\ wt\ \%}$, the conductivity is decoupled over a broad temperature range but at temperatures above ~350 K, the system becomes coupled again as it crosses the ideal line.

As we mentioned above, only a few reports revealed a decoupling phenomenon in classical aprotic ILs.[35,36] The appearance of decoupling in IL−OAPS resembles more the behavior of polymerized ILs (PolyILs). In these materials, one type of ion is covalently attached to the polymer chains, which makes them significantly less mobile than the ion of the opposite charge sign. Several studies[50,51] dealing with the underlying mechanisms of decoupling in PolyILs demonstrated the critical effect of the MW and the chain-like dynamics on the decoupling. Specifically, it was shown that the degree of decoupling increases with the increase in MW of the polymer, while the charge transport of monomers and dimers remains closely coupled to the structural relaxation. However, one critical difference between the PolyILs and ILs is that pure ILs do not display suprastructural dynamics. Thus, the questions arise: why does the addition of OAPS make ion diffusion faster than the structure fluctuations? Could it be that the addition of OAPS initiates a suprastructural arrangement in the low-MW IL?

Reversible Gelation and Molecular Origin of the Decoupling Phenomenon in Nanocomposites. To address this point, we turn to the analysis of rheological spectra that are presented in Figure 7.

As seen here, the mechanical complexity of composites increases with the increase in the OAPS concentration. At low frequencies or high temperatures, the presence of the terminal relaxation mode manifesting itself as $G'(\omega) \sim \omega^2$ and $G''(\omega) \sim \omega$ is observed for all composites presented in Figure 7A. Although IL−OAPS$^{50\ wt\ \%}$ G' and G'' could not be monitored because of the high stiffness of the sample, the creep compliance, $J(t)$, presented in the inset of Figure 7A demonstrates that even in this composite, the final flow regime can be reached as the slope at a longer time is nearly unity. The presence of this terminal flow regime at high T reveals that the present composites are heat-processable. This property differentiates them from the conventional polymer electrolyte composites with bigger filler sizes.[15]

Further examination of the rheological spectra presented in Figure 7A reveals that in both IL−OAPS$^{10\ wt\ \%}$ and the IL−OAPS$^{30\ wt\ \%}$, the structural relaxation peak is separated from the terminal relaxation mode by several orders of magnitude, implying the presence of supramolecular dynamics which contribute to the overall mechanical spectra of these materials.

https://dx.doi.org/10.1021/acsami.0c08323
ACS Appl. Mater. Interfaces 2020, 12, 31842−31851

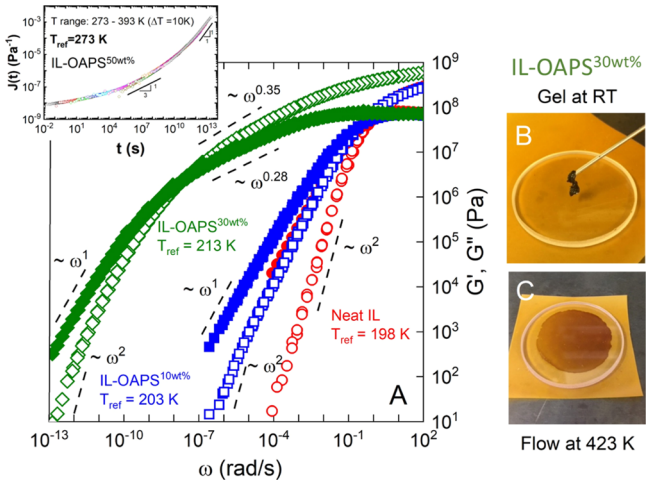

Figure 7. (A) Linear viscoelastic master curves of IL−OAPS nanocomposites with different loadings. The open symbols represent the storage modulus, $G'(\omega)$, and the filled symbols are the loss modulus, $G''(\omega)$. The master curves have been constructed using the frequency−temperature superposition at reference temperatures of T_{ref} = 198 K for neat IL, T_{ref} = 203 K for IL−OAPS$^{10\ wt\ \%}$, and T_{ref} = 213 K for IL−OAPS$^{30\ wt\ \%}$. The inset represents the creep master plot for IL−OAPS$^{50\ wt\ \%}$ nanocomposites. Photographs of IL−OAPS$^{30\ wt\ \%}$ at RT (B) and after heating to 423 K (C).

In particular, for IL−OAPS$^{30\ wt\ \%}$, the intermediate relaxation regime spans between the terminal relaxation frequency $1/\tau_\tau \sim 10^{-12}$ rad/s and the structural relaxation frequency at $1/\tau_\alpha \sim 10^{-1}$ rad/s.

The evolution of the rheological spectra of IL mixed with OAPS resembles that of PolyILs where the appearance of intermediate relaxations is associated with the chain-like relaxation governed by the polymer MW. However, because the neat IL does not exhibit any chain-like relaxation, the presently uncovered supramolecular relaxations should be associated with the development of long-relaxing structural features triggered by the addition of OAPS. To get some insights into the type of structural organization in the composites, we analyzed the spectral shape of the intermediate frequency regions. In the case of IL−OAPS$^{10\ wt\ \%}$, $G'(\omega) \sim \omega^1$ is observed at the intermediate frequency region which points out to the absence of gelation[52] but suggests a presence of rather large slowly relaxing clusters. In IL−OAPS$^{30\ wt\ \%}$, intermediate frequencies G' and G'' display a weak power-law dependence $G'(\omega) \sim \omega^{0.35}$ and $G''(\omega) \sim \omega^{0.28}$ that is the characteristic of gel-like dynamics.[52] The presence of the region $J(t) \sim t^{1/3}$ spanning over 3 decades in the intermediate time (inset Figure 7A) suggests a presence of supramolecular relaxation and gel-like dynamics also in IL−OAPS$^{50\ wt\ \%}$. The photographs of the gel-like structure of IL−OAPS$^{30\ wt\ \%}$ made at room temperature (RT) are presented in Figure 7B. The presence of a terminal relaxation mode at high T for these samples manifesting as $G'(\omega) \sim \omega^2$ and $G''(\omega) \sim \omega$ for IL−OAPS$^{30\ wt\ \%}$ and $J(t) \sim t^1$ for IL−OAPS$^{50\ wt\ \%}$ reflects the reversible nature of the gel-like network in the intermediate frequency region. The photograph demonstrating that IL−OAPS$^{30\ wt\ \%}$ flows at high temperature is presented in Figure 7C. Similar effects of the reversible gelation have been reported in the literature for various systems associating through noncovalent interactions.[53,54] In our case, we hypothesize that the transient supramolecular assemblies might originate from the hydrogen bond formation in composites.

To identify the presence and evolution of the hydrogen bonds in the composite, we probed the N−H stretching region (3150−3550 cm^{-1}) in the FTIR spectra versus temperature. Figure 8 shows the N−H stretching region of samples IL−

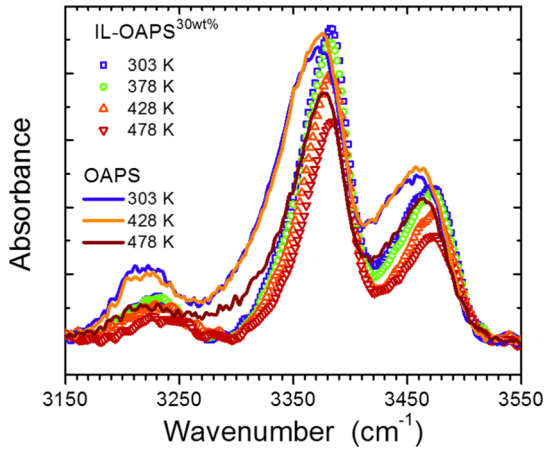

Figure 8. NH-stretch region of IL−OAPS$^{30\ wt\ \%}$ (empty symbols) and OAPS (solids lines) measured at different temperatures by FTIR. The absorbance of samples is scaled with the concentration of OAPS.

OAPS$^{30\ wt\ \%}$ (empty symbols) and OAPS (solid lines). Following extensive reports on hydrogen bonding in the aniline-based system, we assign major peaks at ∼3375 and 3473 cm^{-1} to the NH2 symmetric and asymmetric stretches.[55,56] The feature at ∼3230 cm^{-1} is related to N−H hydrogen bonding, specifically the presence of NH···N interactions.[55,56] For the IL−OAPS$^{30\ wt\ \%}$ system, the overall peak intensities decrease with increasing temperature including the peak at 3230 cm^{-1}. Notably, for the symmetric stretch, it is observed that the low-frequency side of the peak decreases with temperature and results in peak narrowing. Given that hydrogen bonding tends to broaden related spectral signatures, the apparent peak narrowing suggests that the extent of H-bonding decreases with increasing temperature. For neat OAPS, the similar temperature dependence of the N−H stretches is found. Here, the peak positions are red-shifted compared to the spectra of the composite. The red-shifting suggests that the H-bonds within the composite are weaker compared to the neat OAPS sample. Also, the peak at 3230 cm^{-1} is substantially weaker in the composite, suggesting a possible substitution of strong OAPS−OAPS interactions by weaker IL−OAPS hydrogen bonds. Determining exactly which species are interacting with the heterocyclic amine is challenging only using the broad H-bond signatures; however, from the chemical standpoint, electronegativity of atoms (O, N, and F) in TFSI ion favors the formation of hydrogen bonds with OAPS comparing to more positive ammonium ions.

The results of rheological (Figure 7) and FTIR (Figure 8) measurement suggest the presence of hydrogen bonds that are involved in the formation of the clusters at low OAPS loading. At a higher concentration of OAPS, the clusters tend to percolate yielding extended network-like structures with intrinsic dynamics evident from rheological measurements (Figure 7). The possible structural units containing TFSI are presented in Scheme 1. As demonstrated in Scenario 2, in the case of high OAPS concentration, stronger TFSI localization is expected.

https://dx.doi.org/10.1021/acsami.0c08323
ACS Appl. Mater. Interfaces 2020, 12, 31842−31851

Scheme 1. Possible Mechanisms of Immobilization of Anions by OAPS

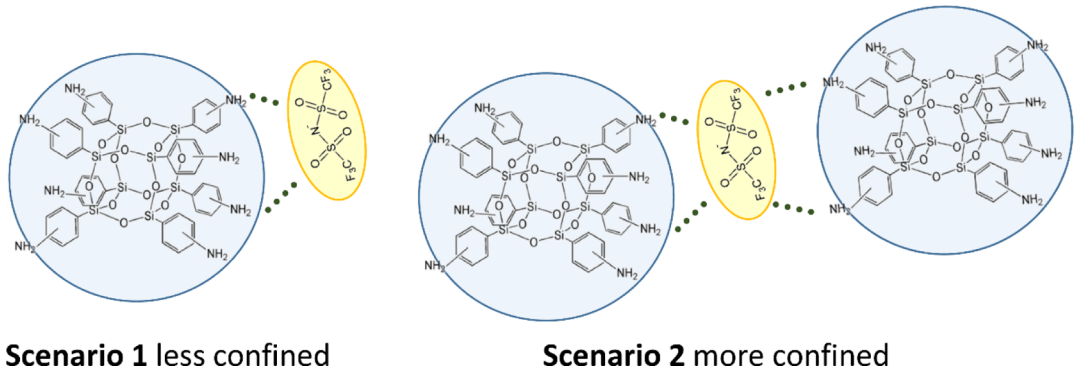

Effect of a Structural Network on the Transport Number and Decoupling Phenomenon. As can be seen from Scheme 1, the hydrogen-bond-induced localization of TFSI in the cluster and/or as a part of the network could ultimately lead to weakening of the electrostatic interaction within the IL's ionic pairs. This may affect both the ions' dissociation and their diffusivities. In this context, the important question to address is how the structural network formation impacts the diffusion coefficients of the individual ions in ILs.

To address this question, we calculated the transport number for pure IL and mixtures with 10 and 30 wt % of OAPS NPs. The transport numbers of the two types of ions are determined as $t_{+/-} = D_{+/-}/(D_+ + D_-)$ where D_+ and D_- denote the diffusion coefficients of cations and anions, respectively, both obtained from PFG-NMR measurements (Figure 5B). The temperature evolution of the transport number for N_{2288} cations (t_+) is presented in Figure 9.

In the temperature interval from 300 to 350 K, t_+ increases with the increase in OAPS concentration. In this temperature range, the stronger contribution of cations to the overall diffusion indicates that the network formation evidenced from rheology slows down (cages) the anions through the H-bonded aggregates, as depicted in Scheme 1 (Scenario 1). This effect is amplified by the increase in OAPS concentration (Scheme 1, Scenario 2), which makes anions even less mobile. This is the case for the IL−OAPS$^{30\ wt\ \%}$ mixture where the slowing down of anions results in complete switching in the rate of the diffusion of the ions and significant enhancement in t_+ compared to that the pure IL and IL−OAPS$^{10\ wt\ \%}$. Specifically, at ∼313 K, t_+ in IL−OAPS$^{30\ wt\ \%}$ reaches the value of 0.62, which is about 40% higher than that of the pure IL. The interaction between the anion and OAPS reduces not only the mobility of the anion but also possibly decreases electrostatic interaction in ion pair which leads to enhancement in the cation diffusion. The possible mechanism of diffusion of ions at low T is presented in Scheme 2.

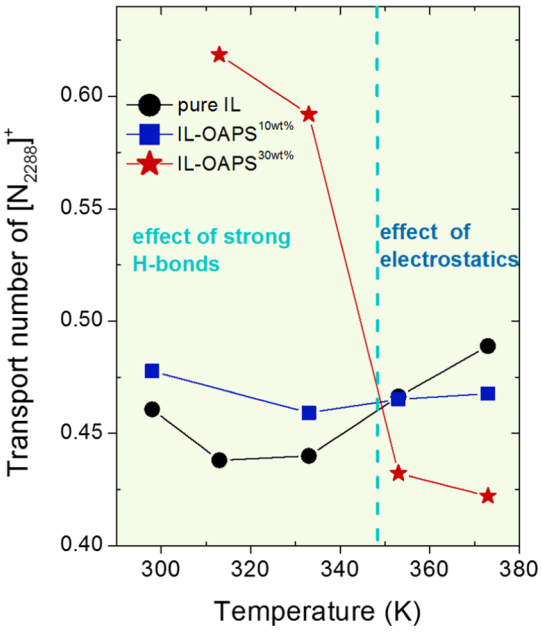

Figure 9. Temperature dependence of the transport number calculated for cations.

At temperatures above 350 K, the anion diffuses faster than the cation, resembling the diffusion behavior of the pure IL (Figure 5B). In this temperature interval, the terminal relaxation regimes that are present in the rheological spectra of all composites suggest that the H-bonded network is significantly weakened, which leads to dissociation of the anion from the network, enhancing its contribution to overall diffusion. The mechanism of diffusion for the high T region is also sketched in Scheme 2.

The observed effective "on" and "off" switching of the network via the temperature and the concentration of NPs permits modulation of the diffusion of ions and enables control over transport properties.

It is important to mention that the observed slowing down of the anions at the low-temperature limit also triggers the decoupling of ion transport from structural relaxation, and is especially noticeable in IL−OAPS$^{30\ wt\ \%}$. This is visible from both the Walden plot analysis (Figure 6B) and the behavior of the transport number (Figure 9). Indeed, the Walden plot of IL−OAPS$^{30\ wt\ \%}$ crosses the ideal line at high T (at ∼350 K the steady-state viscosity ∼10^{-2} Pa·s) (Figure 6B), and the turning point in the behavior of the transport number for IL−OAPS$^{30\ wt\ \%}$ also occurs at about 350 K. Therefore, below 350 K, the cation diffusion is decoupled from the viscosity while anions are slowed down by a supramolecular network. At temperatures above 350 K, the reorganization and disappearance of the network restore the diffusive pattern of the pure IL where diffusion is governed by (hence coupled to) the segmental relaxation which is highlighted by the Walden plot. In this sense, the effective incorporation of the anion into the network leads to (i) a decrease in its mobility and (ii) an improvement in ions dissociation by reducing an electrostatic interaction in ion-counterion pairs (Scheme 1). Both these

https://dx.doi.org/10.1021/acsami.0c08323
ACS Appl. Mater. Interfaces 2020, 12, 31842−31851

Scheme 2. Sketched Mechanism of Network Formation and the Way It Affects the Diffusion of Ions at Different Temperatures

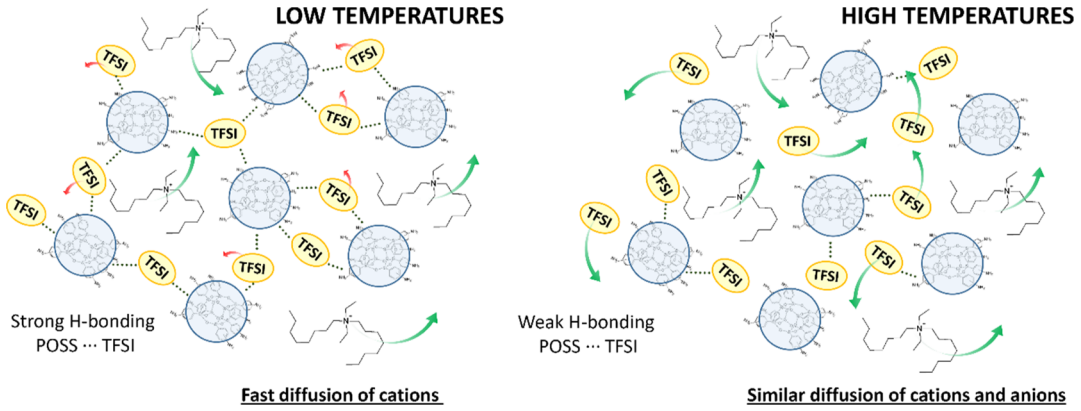

effects enhance the relative diffusion of the cation and promote its decoupling from the fluctuations of the suprastructural network.

SUMMARY

Combining conductivity, rheology, FTIR, and NMR diffusivity results, we demonstrate that the addition of ultrasmall NPs to an IL results in an enhancement of the transport number of the cation by ∼40% at 40 °C. We associate the observed increase with the surface chemistry of NPs that is capable of selective hydrogen bond formation with the anion, slowing down the diffusion of the latter close to RT. The anion−OAPS association is evident from the presence of supramolecular dynamics in rheology and FTIR measurements and the diffusive behavior monitored via PFG-NMR. In particular, at ambient temperature, selective enhancement of the *cation* diffusion through suppression of *anion diffusion* with the increase in OAPS concentrations were observed. At a given critical NP concentration, the cation diffusion coefficient exceeded that of the anion which varies from the diffusive behavior of the two ions in the pure IL. The crossover in diffusivity coincides with the onset of the dynamical decoupling between the charge transport and the structural relaxation, with the cations diffusing faster than the the timescale for structural fluctuations. At high temperatures, the anion−OAPS interaction weakens and the diffusion of anions became faster than that of cations, resembling the trivial diffusive behavior of the pure IL. The transient nature of the supramolecular network, observed from the diffusive behavior and reflected in the rheological measurements, suggests technology-desired processability of composites even for a high concentration of OAPS, thus distinguishing our system from conventional polymer composites with larger fillers' sizes. Our results demonstrate that the formation of transient supramolecular networks can be an effective strategy toward designing melt-processable composites with improved transport number of cations at RT. Furthermore, because of the widespread use of TFSI-based ILs in modern energy-storage technologies, our approach provides a path to control ion diffusion which is important for battery technology.

AUTHOR INFORMATION

Corresponding Authors

Vera Bocharova − *Chemical Sciences Division, Oak Ridge National Laboratory, Oak Ridge, Tennessee 37831, United States;* orcid.org/0000-0003-4270-3866; Email: bocharovav@ornl.gov

Zaneta Wojnarowska − *Chemical Sciences Division, Oak Ridge National Laboratory, Oak Ridge, Tennessee 37831, United States; Institute of Physics, The University of Silesia in Katowice, 41-500 Chorzow, Poland;* orcid.org/0000-0002-7790-2999; Email: zaneta.wojnarowska@smcebi.edu.pl

Authors

Nishani Jayakody − *Department of Physics & Astronomy, Hunter College of the City University of New York, New York, New York 10065, United States*

Jie Yang − *Department of Chemical Engineering and Materials Science, Michigan State University, East Lansing, Michigan 48864, United States; College of Polymer Science and Engineering, Sichuan University, Chengdu, Sichuan 610065, People's Republic of China*

Robert L. Sacci − *Chemical Sciences Division, Oak Ridge National Laboratory, Oak Ridge, Tennessee 37831, United States;* orcid.org/0000-0002-0073-5221

Wei Yang − *College of Polymer Science and Engineering, Sichuan University, Chengdu, Sichuan 610065, People's Republic of China;* orcid.org/0000-0003-0198-1632

Shiwang Cheng − *Department of Chemical Engineering and Materials Science, Michigan State University, East Lansing, Michigan 48864, United States;* orcid.org/0000-0001-7396-4407

Benjamin Doughty − *Chemical Sciences Division, Oak Ridge National Laboratory, Oak Ridge, Tennessee 37831, United States;* orcid.org/0000-0001-6429-9329

Steven Greenbaum − *Department of Physics & Astronomy, Hunter College of the City University of New York, New York, New York 10065, United States;* orcid.org/0000-0001-5497-5274

Seung Pyo Jeong − *Chemical Sciences Division, Oak Ridge National Laboratory, Oak Ridge, Tennessee 37831, United States*

Ivan Popov − *Chemical Sciences Division, Oak Ridge National Laboratory, Oak Ridge, Tennessee 37831, United States*

Sheng Zhao − *Department of Chemistry, University of Tennessee, Knoxville, Tennessee 37996, United States*

Catalin Gainaru − *Fakultät Physik, Technische Universität Dortmund, 44221 Dortmund, Germany;* orcid.org/0000-0001-8295-6433

Complete contact information is available at: https://pubs.acs.org/10.1021/acsami.0c08323

https://dx.doi.org/10.1021/acsami.0c08323
ACS Appl. Mater. Interfaces 2020, 12, 31842−31851

Author Contributions

The manuscript was written through the contributions of all authors. All authors have approved the final version of the manuscript.

Notes

The authors declare no competing financial interest.

■ ACKNOWLEDGMENTS

This work was supported by Laboratory Directed Research and Development program of Oak Ridge National Laboratory, managed by UT-Battelle, LLC, for the U.S. Department of Energy. I.P. and R.L.C. acknowledge the partial financial support by the U.S. Department of Energy (DOE), Office of Science, Basic Energy Sciences, Materials Sciences and Engineering Division for data analysis and FTIR measurements. B.D. was supported by the U.S. Department of Energy, Office of Science, Basic Energy Sciences, Chemical Sciences, Geosciences, and Biosciences Division. N.J. and S.G. acknowledge support from the U.S. Office of Naval Research, grant # N00014-20-1-2186. C.G. acknowledges financial support from Deutsche Forschungsgemeinschaft under GA2680/1-1 project.

■ REFERENCES

(1) Frömling, T.; Kunze, M.; Schönhoff, M.; Sundermeyer, J.; Roling, B. Enhanced Lithium Transference Numbers in Ionic Liquid Electrolytes. *J. Phys. Chem. B* **2008**, *112*, 12985−12990.

(2) Valøen, L. O.; Reimers, J. N. Transport Properties of Lipf6-Based Li-Ion Battery Electrolytes. *J. Electrochem. Soc.* **2005**, *152*, A882−A891.

(3) Mindemark, J.; Lacey, M. J.; Bowden, T.; Brandell, D. Beyond Peo—Alternative Host Materials for Li^+-Conducting Solid Polymer Electrolytes. *Prog. Polym. Sci.* **2018**, *81*, 114−143.

(4) Zhang, H.; Li, C.; Piszcz, M.; Coya, E.; Rojo, T.; Rodriguez-Martinez, L. M.; Armand, M.; Zhou, Z. Single Lithium-Ion Conducting Solid Polymer Electrolytes: Advances and Perspectives. *Chem. Soc. Rev.* **2017**, *46*, 797−815.

(5) Lago, N.; Garcia-Calvo, O.; Lopez del Amo, J. M.; Rojo, T.; Armand, M. All-Solid-State Lithium-Ion Batteries with Grafted Ceramic Nanoparticles Dispersed in Solid Polymer Electrolytes. *ChemSusChem* **2015**, *8*, 3039−3043.

(6) Kumar, B.; Scanlon, L. G. Polymer-Ceramic Composite Electrolytes. *J. Power Sources* **1994**, *52*, 261.

(7) Croce, F.; Appetecchi, G. B.; Persi, L.; Scrosati, B. Nanocomposite Polymer Electrolytes for Lithium Batteries. *Nature* **1998**, *394*, 456.

(8) Manuel Stephan, A.; Nahm, K. S. Review on Composite Polymer Electrolytes for Lithium Batteries. *Polymer* **2006**, *47*, 5952.

(9) Nairn, K.; Forsyth, M.; Every, H.; Greville, M.; MacFarlane, D. R. Polymer-Ceramic Ion-Conducting Composites. *Solid State Ionics* **1996**, *86*−*88*, 589.

(10) Wieczorek, W.; Florjanczyk, Z.; Stevens, J. R. Composite Polyether Based Solid Electrolytes. *Electrochim. Acta* **1995**, *40*, 2251.

(11) Wieczorek, W.; Stevens, J. R.; Florjańczyk, Z. Composite Polyether Based Solid Electrolytes. The Lewis Acid-Base Approach. *Solid State Ionics* **1996**, *85*, 67.

(12) Yang, T.; Zheng, J.; Cheng, Q.; Hu, Y.-Y.; Chan, C. K. Composite Polymer Electrolytes with Li7la3zr2o12 Garnet-Type Nanowires as Ceramic Fillers: Mechanism of Conductivity Enhancement and Role of Doping and Morphology. *ACS Appl. Mater. Interfaces* **2017**, *9*, 21773−21780.

(13) Chen, G.; Niu, C.; Chen, Y.; Shang, W.; Qu, Y.; Du, Z.; Zhao, L.; Liao, X.; Du, J.; Chen, Y. A Single-Ion Conducting Polymer Electrolyte Based on Poly(Lithium 4-Styrenesulfonate) for High-Performance Lithium Metal Batteries. *Solid State Ionics* **2019**, *341*, 115048.

(14) Nguyen, H.-D.; Kim, G.-T.; Shi, J.; Paillard, E.; Judeinstein, P.; Lyonnard, S.; Bresser, D.; Iojoiu, C. Nanostructured Multi-Block Copolymer Single-Ion Conductors for Safer High-Performance Lithium Batteries. *Energy Environ. Sci.* **2018**, *11*, 3298−3309.

(15) Yao, P.; Yu, H.; Ding, Z.; Liu, Y.; Lu, J.; Lavorgna, M.; Wu, J.; Liu, X. Review on Polymer-Based Composite Electrolytes for Lithium Batteries. *Front. Chem.* **2019**, *7*, 522.

(16) Croce, F.; Curini, R.; Martinelli, A.; Persi, L.; Ronci, F.; Scrosati, B.; Caminiti, R. Physical and Chemical Properties of Nanocomposite Polymer Electrolytes. *J. Phys. Chem. B* **1999**, *103*, 10632−10638.

(17) Croce, F.; Settimi, L.; Scrosati, B. Superacid ZrO_2-Added, Composite Polymer Electrolytes with Improved Transport Properties. *Electrochem. Commun.* **2006**, *8*, 364−368.

(18) Tominaga, Y.; Endo, M. Ion-Conductive Properties of Polyether-Based Composite Electrolytes Filled with Mesoporous Silica, Alumina and Titania. *Electrochim. Acta* **2013**, *113*, 361−365.

(19) Kato, T.; Kado, T.; Tanaka, S.; Okazaki, A.; Hayase, S. Quasi-Solid Dye-Sensitized Solar Cells Containing Nanoparticles Modified with Ionic Liquid-Type Molecules. *J. Electrochem. Soc.* **2006**, *153*, A626.

(20) Ma, P.; Fang, Y.; Zhang, D.; Cheng, H.; Fu, N.; Zhou, X.; Fang, S.; Lin, Y. Surface Functionalization of TiO_2 Nanoparticles Influences the Conductivity of Ionic Liquid-Based Composite Electrolytes. *ACS Appl. Nano Mater.* **2020**, *3*, 342−350.

(21) Cheng, S.; Xie, S.-J.; Carrillo, J.-M. Y.; Carroll, B.; Martin, H.; Cao, P.-F.; Dadmun, M. D.; Sumpter, B. G.; Novikov, V. N.; Schweizer, K. S.; Sokolov, A. P. Big Effect of Small Nanoparticles: A Shift in Paradigm for Polymer Nanocomposites. *ACS Nano* **2017**, *11*, 752−759.

(22) Romero-Guzmán, M. E.; Romo-Uribe, A.; Zárate-Hernández, B. M.; Cruz-Silva, R. Viscoelastic Properties of Poss−Styrene Nanocomposite Blended with Polystyrene. *Rheol. Acta* **2009**, *48*, 641−652.

(23) Murch, G. The Haven Ratio in Fast Ionic Conductors. *Solid State Ionics* **1982**, *7*, 177.

(24) Kuwata, N.; Lu, X.; Miyazaki, T.; Iwai, Y.; Tanabe, T.; Kawamura, J. Lithium Diffusion Coefficient in Amorphous Lithium Phosphate Thin Films Measured by Secondary Ion Mass Spectroscopy with Isotope Exchange Methods. *Solid State Ionics* **2016**, *294*, 59−66.

(25) Marcolongo, A.; Marzari, N. Ionic Correlations and Failure of Nernst-Einstein Relation in Solid-State Electrolytes. *Phys. Rev. Mater.* **2017**, *1*, 025402.

(26) Imrie, C. T.; Ingram, M. D.; McHattie, G. S. Ion Transport in Glassy Polymer Electrolytes. *J. Phys. Chem. B* **1999**, *103*, 4132−4138.

(27) Wang, Y.; Fan, F.; Agapov, A. L.; Yu, X.; Hong, K.; Mays, J.; Sokolov, A. P. Design of Superionic Polymers—New Insights from Walden Plot Analysis. *Solid State Ionics* **2014**, *262*, 782−784.

(28) Wang, Y.; Fan, F.; Agapov, A. L.; Saito, T.; Yang, J.; Yu, X.; Hong, K.; Mays, J.; Sokolov, A. P. Examination of the Fundamental Relation between Ionic Transport and Segmental Relaxation in Polymer Electrolytes. *Polymer* **2014**, *55*, 4067−4076.

(29) Sangoro, J. R.; Iacob, C.; Agapov, A. L.; Wang, Y.; Berdzinski, S.; Rexhausen, H.; Strehmel, V.; Friedrich, C.; Sokolov, A. P.; Kremer, F. Decoupling of Ionic Conductivity from Structural Dynamics in Polymerized Ionic Liquids. *Soft Matter* **2014**, *10*, 3536−3540.

(30) Nakamura, K.; Fukao, K. Dielectric Relaxation Behavior of Polymerized Ionic Liquids with Various Charge densities. *Polymer* **2013**, *54*, 3306−3313.

(31) Fan, F.; Wang, Y.; Hong, T.; Heres, M. F.; Saito, T.; Sokolov, A. P. Ion Conduction in Polymerized Ionic Liquids with Different Pendant Groups. *Macromolecules* **2015**, *48*, 4461−4470.

(32) Sasabe, H.; Saito, S. Relationship between Ionic Mobility and Segmental Mobility in Polymers in the Liquid State. *Polym. J.* **1972**, *3*, 624−630.

(33) Choi, U. H.; Ye, Y.; Salas de la Cruz, D.; Liu, W.; Winey, K. I.; Elabd, Y. A.; Runt, J.; Colby, R. H. Dielectric and Viscoelastic

https://dx.doi.org/10.1021/acsami.0c08323
ACS Appl. Mater. Interfaces 2020, 12, 31842−31851

Responses of Imidazolium-Based Ionomers with Different Counterions and Side Chain Lengths. *Macromolecules* **2014**, *47*, 777−790.
(34) Wojnarowska, Z.; Feng, H.; Fu, Y.; Cheng, S.; Carroll, B.; Kumar, R.; Novikov, V. N.; Kisliuk, A. M.; Saito, T.; Kang, N.-G.; Mays, J. W.; Sokolov, A. P.; Bocharova, V. Effect of Chain Rigidity on the Decoupling of Ion Motion from Segmental Relaxation in Polymerized Ionic Liquids: Ambient and Elevated Pressure Studies. *Macromolecules* **2017**, *50*, 6710.
(35) Griffin, P.; Agapov, A. L.; Kisliuk, A.; Sun, X.-G.; Dai, S.; Novikov, V. N.; Sokolov, A. P. Decoupling Charge Transport from the Structural Dynamics in Room Temperature Ionic Liquids. *J. Chem. Phys.* **2011**, *135*, 114509.
(36) Griffin, P. J.; Agapov, A. L.; Sokolov, A. P. Translation-Rotation Decoupling and Nonexponentiality in Room Temperature Ionic Liquids. *Phys. Rev. E: Stat., Nonlinear, Soft Matter Phys.* **2012**, *86*, 021508.
(37) Wagner, H.; Richert, R. Equilibrium and Non-Equilibrium Type B-Relaxations: D-Sorbitol Versus O-Terphenyl. *J. Phys. Chem. B* **1999**, *103*, 4071−4077.
(38) Fan, F.; Wang, Y.; Sokolov, A. P. Ionic Transport, Microphase Separation, and Polymer Relaxation in Poly(Propylene Glycol) and Lithium Perchlorate Mixtures. *Macromolecules* **2013**, *46*, 9380−9389.
(39) Samet, M.; Levchenko, V.; Boiteux, G.; Seytre, G.; Kallel, A.; Serghei, A. Electrode Polarization Vs. Maxwell-Wagner-Sillars Interfacial Polarization in Dielectric Spectra of Materials: Characteristic Frequencies and Scaling Laws. *J. Chem. Phys.* **2015**, *142*, 194703.
(40) Ferry, J. D. *Viscoelastic Properties of Polymers*; Wiley: New York, 1980.
(41) Dong, K.; Liu, X.; Dong, H.; Zhang, X.; Zhang, S. Multiscale Studies on Ionic Liquids. *Chem. Rev.* **2017**, *117*, 6636−6695.
(42) Hayes, R.; Warr, G. G.; Atkin, R. Structure and Nanostructure in Ionic Liquids. *Chem. Rev.* **2015**, *115*, 6357−6426.
(43) Sangoro, J.; Iacob, C.; Serghei, A.; Naumov, S.; Galvosas, P.; Kärger, J.; Wespe, C.; Bordusa, F.; Stoppa, A.; Hunger, J.; Buchner, R.; Kremer, F. Electrical Conductivity and Translational Diffusion in the 1-Butyl-3-Methylimidazolium Tetrafluoroborate Ionic Liquid. *J. Chem. Phys.* **2008**, *128*, 214509.
(44) Musiał, M.; Wojnarowska, Z.; Cheng, S.; Ngai, K. L.; Paluch, M. Evidence of a Fundamental Mechanism Governing Conductivity Relaxation in Room-Temperature Ionic Liquid. *J. Phys. Chem. C* **2019**, *123*, 22089−22094.
(45) Wojnarowska, Z.; Thoms, E.; Blanchard, B.; Tripathy, S. N.; Goodrich, P.; Jacquemin, J.; Knapik-Kowalczuk, J.; Paluch, M. How Is Charge Transport Different in Ionic Liquids? The Effect of High Pressure. *Phys. Chem. Chem. Phys.* **2017**, *19*, 14141−14147.
(46) Mizuno, F.; Belieres, J.-P.; Kuwata, N.; Pradel, A.; Ribes, M.; Angell, C. A. Highly Decoupled Ionic and Protonic Solid Electrolyte Systems, in Relation to Other Relaxing Systems and Their Energy Landscapes. *J. Non-Cryst. Solids* **2006**, *352*, 5147−5155.
(47) Ingram, M. D. Ionic Conductivity and Glass Structure. *Philos. Mag. B* **1989**, *60*, 729−740.
(48) Angell, C. Fast Ion Motion in Glassy and Amorphous Materials. *Solid State Ionics* **1983**, *9−10*, 3−16.
(49) Ohno, H. *Electrochemical Aspects of Ionic Liquids*; John Wiley & Sons, Inc., 2005.
(50) Fan, F.; Wang, W.; Holt, A. P.; Feng, H.; Uhrig, D.; Lu, X.; Hong, T.; Wang, Y.; Kang, N.-G.; Mays, J.; Sokolov, A. P. Effect of Molecular Weight on the Ion Transport Mechanism in Polymerized Ionic Liquids. *Macromolecules* **2016**, *49*, 4557−4570.
(51) Wieland, F.; Bocharova, V.; Münzner, P.; Hiller, W.; Sakrowski, R.; Sternemann, C.; Böhmer, R.; Sokolov, A. P.; Gainaru, C. Structure and Dynamics of Short-Chain Polymerized Ionic Liquids. *J. Chem. Phys.* **2019**, *151*, 034903.
(52) Colby, R. H.; Gillmor, J. R.; Rubinstein, M. Dynamics of near-Critical Polymer Gels. *Phys. Rev. E: Stat. Phys., Plasmas, Fluids, Relat. Interdiscip. Top.* **1993**, *48*, 3712−3716.
(53) Huang, C.; Wang, C.; Chen, Q.; Colby, R. H.; Weiss, R. A. Reversible Gelation Model Predictions of the Linear Viscoelasticity of Oligomeric Sulfonated Polystyrene Ionomer Blends. *Macromolecules* **2016**, *49*, 3936−3947.
(54) Chen, Q.; Huang, C.; Weiss, R. A.; Colby, R. H. Viscoelasticity of Reversible Gelation for Ionomers. *Macromolecules* **2015**, *48*, 1221−1230.
(55) Meng-Xia, X.; Yuan, L. Studies on the Hydrogen Bonding of Aniline's Derivatives by FT-IR. *Spectrochim. Acta, Part A* **2002**, *58*, 2817−2826.
(56) Krueger, P. J. The Vibrational Mechanism of the Fundamental NH_2 Stretching Vibrations in Anilines. *Can. J. Chem.* **1962**, *40*, 2300−2316.

https://dx.doi.org/10.1021/acsami.0c08323
ACS Appl. Mater. Interfaces 2020, 12, 31842−31851